

Review

# Impact of Structural Strain in Perovskite Epitaxial Thin Films on Their Functional Properties

Florin Andrei <sup>1</sup>, Maria Dinescu <sup>1</sup>, Valentin Ion <sup>1</sup>, Floriana Craciun <sup>2</sup>, Ruxandra Birjega <sup>1</sup> and Nicu Doinel Scarisoreanu <sup>1,\*</sup>

<sup>1</sup> National Institute for Laser, Plasma and Radiation Physics, Photoplasmat Center (C400) and Laser Department, 409 Atomistilor Street, RO-077125 Magurele, Romania; florin.andrei@infpr.ro (F.A.); dinescum@nipne.ro (M.D.); valentin.ion@infpr.ro (V.I.); ruxandra.birjega@infpr.ro (R.B.)

<sup>2</sup> CNR-ISM, Istituto di Struttura della Materia, Area della Ricerca di Roma-Tor Vergata, Via del Fosso del Cavaliere 100, I-00133 Rome, Italy; floriana.craciun@artov.ism.cnr.it

\* Correspondence: nicu.scarisoreanu@infpr.ro

**Abstract:** The strain engineering effects induced by different means, e.g., the substrate lattice mismatch and/or chemical doping, on the functional properties of perovskite thin films have triggered interest in the use of these materials in different applications such as energy storage/generation or photonics. The effects of the film's thickness and strain state of the structure for the lead-free perovskite ferrite-based materials (BiFeO<sub>3</sub>-BFO; Y-doped BiFeO<sub>3</sub>-BYFO; LaFeO<sub>3</sub>-LFO) on their functional properties are highlighted here. As was previously demonstrated, the dielectric properties of BFO epitaxial thin films are strongly affected by the film thickness and by the epitaxial strain induced by the lattice mismatch between substrate and film. Doping the BiFeO<sub>3</sub> ferroelectric perovskite with rare-earth elements or inducing a high level of structural deformation into the crystalline structure of LaFeO<sub>3</sub> thin films have allowed the tuning of functional properties of these materials, such as dielectric, optical or photocatalytic ones. These changes are presented in relation to the appearance of complex ensembles of nanoscale phase/nanodomains within the epitaxial films due to strain engineering. However, it is a challenge to maintain the same level of epitaxial strain present in ultrathin films (<10 nm) and to preserve or tune the positive effects in films of thicknesses usually higher than 30 nm.

**Keywords:** strain engineering; epitaxial thin films; ferroelectric perovskite thin films



**Citation:** Andrei, F.; Dinescu, M.; Ion, V.; Craciun, F.; Birjega, R.; Scarisoreanu, N.D. Impact of Structural Strain in Perovskite Epitaxial Thin Films on Their Functional Properties. *Crystals* **2023**, *13*, 1686. <https://doi.org/10.3390/cryst13121686>

Academic Editor: Sawanta S. Mali

Received: 27 October 2023

Revised: 11 December 2023

Accepted: 12 December 2023

Published: 14 December 2023



**Copyright:** © 2023 by the authors. Licensee MDPI, Basel, Switzerland. This article is an open access article distributed under the terms and conditions of the Creative Commons Attribution (CC BY) license (<https://creativecommons.org/licenses/by/4.0/>).

## 1. Introduction

Ferroelectricity is the ability of some materials to present spontaneous electric polarization, reversible when an external electric field is applied. The ferroelectric materials undergo spontaneous polarization below a temperature limit called the Curie temperature. Materials having the ability to generate an internal electric field, when a mechanical pressure or strain is applied, are piezoelectric materials. The most known piezoelectric material is lead zirconate titanate Pb(Zr<sub>1-x</sub>Ti<sub>x</sub>)O<sub>3</sub> (PZT), a solid-mixture solution of PbZrO<sub>3</sub> and PbTiO<sub>3</sub> with piezoelectric properties, which generates electrical charges under mechanical stress (direct effect) or produces structural deformation when an electrical field is applied (converse effect) [1]. In the paraelectric state, where no spontaneous polarization and no piezoelectric effects are present, PZT has a cubic ABO<sub>3</sub> crystalline perovskite structure (the same as the initial two compounds), where Pb<sup>2+</sup> ions occupy the A-site, while the B-site is randomly occupied by Zr<sup>4+</sup> and Ti<sup>4+</sup>. For a certain range of compositions, and for temperatures lower than the Curie temperature (T<sub>c</sub>, which can vary from 220 °C to 490 °C, depending on the chemical composition) [2], PZT in the ferroelectric phase exhibits a tetragonal structure, which transforms into a rhombohedral phase by varying the cations' proportion in the solid solution. Compared to the cubic structure, in the tetragonal phase, the octahedron formed by oxygen anions is moved off from the center of the cube

formed by  $\text{Pb}^{2+}$  cations, and the B-site cations in the center of the oxygen octahedron are also shifted [3–5], giving rise to a spontaneous polarization. The direction of the spontaneous polarization changes in the rhombohedral phase. Thus, in the PZT solid solution, a phase boundary between rhombohedral and tetragonal phases (called morphotropic phase boundary) is found in a narrow composition range. According to the results reported by Jaffe et al., the morphotropic phase boundary (MPB) is obtained at room temperature when Ti percentage,  $x$ , equals 48% [2]. The dielectric and piezoelectric properties are maximized at MPB, due to the multiple possible directions allowed for the polarization orientation. PZT-type materials present the maximum absorption of the light in the UV region, having a large band gap, around 3.2–3.7 eV which can differ depending on the composition or the used dopant [6]. In terms of energy production, PZT materials are used, principally, for vibration energy harvesting, where, by applying mechanical/vibrational stress, electrical energy is generated as an effect of the strong piezoelectric properties of this material [1]. However, the main component of PZT (PbO) is toxic, and its toxicity is pronounced because of its volatility at high temperatures during material processing. More than that, Pb is a serious chronic poison with long-term exposure, even in small quantities [7]. It is therefore desired to develop new alternatives of lead-free piezoelectric materials and to transfer them into technologies to substitute PZT compounds.  $\text{BiFeO}_3$  (BFO) is one of the most studied multiferroic materials due to its excellent electrical properties, high Curie temperature ( $T_C \sim 830$  °C) and Néel temperature ( $T_N \sim 370$  °C). It shows a slightly distorted perovskite structure, with a rhombohedral  $R3c$  ground state at room temperature, but it turns into the paraelectric orthorhombic (O)  $Pnma$  phase above  $T_C$  temperature [8]. The highest spontaneous polarization is oriented along the pseudocubic [111] directions and the largest ionic displacements from the centrosymmetric positions are pointed along the same directions. One way to improve the physicochemical properties of BFO is by chemical doping, where generally Bi is replaced by rare earth elements and Fe by transitional metal elements. Recent studies of doped BFO have primarily concentrated on investigating the physicochemical characteristics of thin films where rare earth (RE) elements are incorporated into the BFO structure. Researchers have noted a strong correlation with the ionic radius of the substituted elements. Notably, when considering the average radius of the A-site cations, a structural transition involving the rhombohedral–orthorhombic phases was consistently observed at the same average radius value. This transition was found to be independent of the specific type of rare earth ion used [9–13]. Usually, the substitution of Bi cations leads to a decrease in the leakage current density, which improves the ferroelectric and piezoelectric properties [14–18]. For example, Nb-doped BFO films grown on PtSi substrates by PLD show saturated hysteresis loops with a remnant polarization of  $86.4 \mu\text{C}/\text{cm}^2$  [19]. Smooth surfaces with fine microstructures and low leakage currents were reported for polycrystalline Sm-doped BFO films grown by PLD on Pt electrode/glass substrate. These films show remnant polarization ranging from 66–150  $\mu\text{C}/\text{cm}^2$  [20]. A low leakage current was reported for single-phase Ca and Mn co-doped BFO grown on STO substrates with remnant polarization of  $92.5 \mu\text{C}/\text{cm}^2$  [21].

The strain engineering was also demonstrated to be an excellent method for tailoring the functional properties of different material classes (ferroelectric oxides, nitrides, oxinitrides, etc.) [22–24].

Thus, in Ref. [22], a very large remnant polarization ( $\cong 60 \mu\text{C}/\text{cm}^2$ ) was reported for epitaxial BFO thin films deposited by PLD on SRO/STO. The improved polarization was correlated to the compressive stress induced by the SRO layer [22]. Over the years, numerous strategies were used to improve the electrical properties of BFO thin films, and these results will be discussed in detail in the next sections. Besides its excellent electrical properties, BFO shows enhanced photocatalytic (PC) and photoelectrochemical (PEC) activities. The small value of the direct band gap (2.69–2.71 eV) propels BFO-based devices for use as photocatalysts and photoelectrodes with great capabilities to absorb visible light [25]. It has also the advantage that the self-polarization, which induces the internal electric field,

can improve the charge separation through the chemical potential modulation and surface band-bending, which will further enhance the photoelectrochemical properties [26].

Similar effects on the functional properties have been noted for ferroelectric titanate-based materials. A promising lead-free ferroelectric material is barium titanate ( $\text{BaTiO}_3$ ), a perovskite-type material showing relatively good dielectric, ferroelectric and piezoelectric properties.  $\text{BaTiO}_3$  is the first discovered ferroelectric perovskite oxide material. The ferroelectric phase is formed when the temperature decreases below the Curie temperature, and it changes through several phase transitions, transforming from the cubic (centrosymmetric phase) to tetragonal, orthorhombic and rhombohedral phases. The displacement of  $\text{Ti}^{4+}$  cations and the orientation of the formed spontaneous polarizations are along [001], [101] and [111] directions, when the ferroelectric phase symmetry changes from tetragonal to orthorhombic and rhombohedral, respectively [27]. Moreover, besides these electric properties,  $\text{BaTiO}_3$  has increased thermal and chemical stability and can be used in large application domains. The Curie temperature of  $\text{BaTiO}_3$  is 120 °C. Above this temperature, the material is in the paraelectric state and has a cubic structure stable up to 1460 °C [28]. Different  $\text{BaTiO}_3$ -based materials have been developed by doping with various elements. An example is  $(\text{Ba,Ca})(\text{Zr,Ti})\text{O}_3$  (BCTZ), which has a perovskitic structure similar to  $\text{BaTiO}_3$ . The doping of Ba and Ti sites with Ca and Zr improves the electrical properties, making the resulting material appropriate for applications in energy harvesting, sensing, etc. The BCTZ formula can be easily written as a two end-materials combination, usually as  $(1-x)\text{Ba}(\text{Ti}_{0.8}\text{Zr}_{0.2})\text{O}_{3-x}(\text{Ba}_{0.7}\text{Ca}_{0.3})\text{TiO}_3$ . The morphotropic phase boundary (MPB), where BCTZ shows the highest dielectric, ferroelectric, and piezoelectric properties, is obtained for  $x \cong 0.5$  [8,29,30]. As was previously demonstrated, the dielectric properties of BCTZ epitaxial thin films are strongly affected by the film thickness and by the epitaxial strain induced by the lattice mismatch between substrate and film [31]. For higher thickness values ( $> 35$  nm), the misfit strain relaxes and the tetragonality ratio and dielectric permittivity are heavily affected [32]. While these ferroelectric perovskite materials are briefly mentioned here for completeness, in the following the attention will be focused on other types of lead-free materials, namely  $\text{BiFeO}_3$  and  $\text{LaFeO}_3$ .

Being part of the wide series of rare-earth orthoferrites,  $\text{LaFeO}_3$  (LFO), having at room temperature a distorted perovskite structure, is an interesting material, especially for its various properties including an antiferromagnetic insulator character (with high  $T_N \cong 740$  °C), the coexistence of coupled ferroelectric and antiferromagnetic orderings, and photoelectrochemical activity [33,34]. It shows an orthorhombic symmetry with lattice parameters  $a = 5.557$  Å,  $b = 5.5652$  Å, and  $c = 7.8542$  Å, belonging to the  $Pbmn$  space group [35]. LFO possesses increased photostability, as well as high stability in both reducing and oxidizing chemical media. It was found that the chemical substitution of  $\text{LaFeO}_3$  cations improves its physicochemical features, leading to a material with enhanced electrical conductivity and thermal stability, a large dielectric constant and low dielectric loss, good permittivity, ferroelectricity and piezoelectricity [30,36,37]. The optical band gap ( $E_g \cong 2.07$ ) coupled to the energy bands position of LFO-based materials make them excellent p-type photocathodes for oxygen and water reduction [38–40].

Within this paper, the effects of the film thickness and strain state of the structure for the lead-free perovskite ferrite-based ( $\text{BiFeO}_3$ -BFO; Y-doped  $\text{BiFeO}_3$ -BYFO;  $\text{LaFeO}_3$ -LFO) materials on their functional properties are presented, for different synthesis routes of the thin films.

## 2. Structural and Functional Properties of Lead-Free Ferrite-Based Perovskite Thin Films

### 2.1. $\text{BiFeO}_3$ (BFO)

Bismuth ferrite (BFO) has received substantial attention in the realm of multiferroic materials and stands out as the most extensively studied due to its exceptional ability to simultaneously exhibit polar and magnetic orders at room temperature. This distinctive property has peaked considerable interest for potential applications in areas such as piezoelectric devices, nonvolatile storage technologies, spintronics, and more [9,41]. An

interesting study focused on antiferromagnetic and ferroelectric properties of BFO-based thin films grown on STO substrates by PLD for spintronics devices was reported by Bea et al. [42]. Ultrathin BFO films coupled with Co and  $\text{La}_{2/3}\text{Sr}_{1/3}\text{MnO}_3$  (LSMO) ferromagnetic electrodes were used as tunnel barriers in magnetic tunnel junctions, and a large tunnel magnetoresistance was recorded due to their insulating and ferromagnetic properties [42]. An asymmetric superlattice, with high crystalline quality, made of 10 series of BFO (6 nm)/STO (1–2.5 nm) films grown on Nb-doped STO substrates, was obtained using magnetron sputtering [43]. It was observed that the in-plane strain is very high for samples having the STO sublayer in the 1 and 1.5 nm thickness range and the films start to be much more relaxed for STO thicknesses higher than 1.75 nm. The electrical polarizations of BFO/STO-based superlattices decrease with the increase in the STO sublayer thickness, the highest values being obtained for samples having 1 nm and 1.5 nm of STO. These results were attributed to the highly compressive strained structure and great crystalline quality of samples with very thin STO layers. The piezoelectric coefficient  $d_{33}$  and remnant polarization follow the same trend and decrease with the structural strain, especially for samples having a STO sublayer equal to or thicker than 1.75 nm [43].

Thin films exhibit varied growth patterns depending on the type of collector substrates they are deposited on. The growth mechanism, their surface characteristics, and their physicochemical attributes are significantly influenced by the properties of the substrate they adhere to. The strain observed within the material structure is a consequence of the difference between the lattice constants of the material and the substrate, commonly referred to as a “mismatch.” When a material undergoes epitaxial growth on a substrate, it tends to conform to the symmetry of the substrate. In the case of a crystalline substrate with a lattice constant ( $a_s$ ) greater than that of the growing material ( $a_m$ ), the growth results in tensile strain. To achieve a perfectly elastic system, the out-of-plane parameter decreases while maintaining the unit cell volume unchanged. Conversely, when  $a_s < a_m$ , a compressive strain occurs, causing the out-of-plane parameter to increase [44,45]. An interesting study related to the influence of the substrate on the optical and structural properties of BFO grown by PLD was reported by Himcinschi et al. The authors have grown BFO films having different thicknesses on STO, Nb-doped STO and  $\text{DyScO}_3$  (DSO) [44]. Clear interference fringes were observed for a thin BFO film grown on a STO substrate, meaning that the film is fully strained, and by increasing the film thickness, the strain is relaxed [46–48]. On the other hand, the behavior of thick BFO film grown on a DSO substrate follows a completely different trend, the film remaining epitaxially strained even at 135 nm thickness. This happens due to the lower difference between the lattice constants of BFO (3.96 Å) and DSO (3.951 Å) compared to STO (3.905 Å) [22,46,49]. A similar feature was reported for BFO films grown on  $\text{LaAlO}_3$  (LAO) substrates (lattice constant of LAO  $\sim$  3.80 Å) with the presence of a large compressive strain even for thicker films (118 nm) [50]. Series of thin films made of BFO,  $\text{BiFeO}_3/\text{NiFe}_2\text{O}_4$  (BFO/NFO),  $\text{BiFe}_{0.94}\text{Mn}_{0.04}\text{O}_3/\text{NiFe}_2\text{O}_4$  (BFMO/NFO) and  $\text{BiFe}_{0.94}\text{Mn}_{0.04}\text{Cr}_{0.02}\text{O}_3/\text{NiFe}_2\text{O}_4$  (BFMCO/NFO) were grown by sol-gel on FTO/glass substrates [51].

A massive structural distortion from rhombohedral to tetragonal phases is observed for BFMO/NFO and BFMCO/NFO samples, these samples having the highest structural stress because of the ion doping and the structural transformation. The highest ferroelectricity and the lowest leakage current density is observed for the same samples, meaning that the structural strain strongly affects their physicochemical properties [51]. BFO films with thicknesses ranging from 1 nm to 150 nm were deposited on STO substrates with a bottom layer of LSMO through PLD, and their structural and piezoelectric properties were studied in detail [52]. It was found that the structural strain of BFO-based films is almost constant for thicknesses  $\leq$  30 nm, but the structure starts to be relaxed above this thickness. The piezoelectric coefficient  $d_{33}$  slowly decreases with the film thickness decrease due to the clamping effect of the substrate to the film and depolarization [52].

High-quality epitaxial BFO and Y-doped BFO (Y-BFO;  $\text{Bi}_{0.95}\text{Y}_{0.05}\text{FeO}_3$ ) films were grown on STO substrates through the PLD technique [9]. The Y-BFO film shows the out-

of-plane parameter (4.0042 Å) slightly larger than that obtained for BFO film (3.9983 Å). The in-plane parameter of Y-BFO (3.9266 Å) is quite close to the lattice parameter of the cubic substrate (3.905 Å). The compressive in-plane strain induced by the STO substrate is responsible for the difference between the out-of-plane and in-plane parameters because the cell is expanded in the out-of-plane direction (monoclinic distortion). This monoclinic distortion is also evidenced by the rocking curve measurements, where the full width at half maximum (FWHM) values appears to be larger for Y-BFO films compared to those obtained for BFO films. The formation of an interesting tilted-stripe nanodomain structure, where the compressive and tensile strains alternate, was evidenced for Y-BFO films, they being absent for pure BFO films. Huge in-plane dielectric permittivity ( $\cong 2500$ ) and low dielectric loss ( $<0.01$ ) were obtained for Y-BFO films, and these excellent features were attributed to the appearance of a complex stripe nanodomain structure with monoclinic symmetry and to the chemical doping [9]. Values of dielectric permittivity obtained for Y-BFO films are much higher than values obtained for (undoped) BFO films and similar to those obtained for BCTZ 45  $((1-x)\text{Ba}(\text{Ti}_{0.8}\text{Zr}_{0.2})\text{TiO}_3 - x(\text{Ba}_{0.7}\text{Ca}_{0.3})\text{TiO}_3, x = 0.45$  (BCZT 45)) films with appropriate thicknesses, as can be seen in Figure 1. It is clear that the epitaxial strain plays an important role in the improvement of the dielectric behavior of different types of lead-free ferroelectric materials, as depicted in Figure 1. However, the addition of chemical pressure due to a dopant within the BFO thin film structure will induce supplementary constraints on the crystalline structure of the BFO film, leading to the appearance of peculiar “stripe-looking” nanodomains which are enhancing the dielectric response of the Y-BFO films [9].

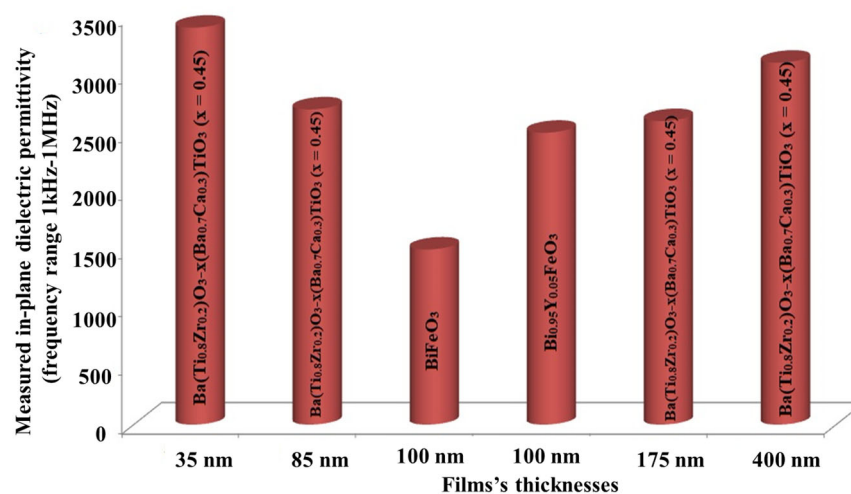


**Figure 1.** Measured in-plane dielectric permittivity of BCTZ 45, BFO and Y-doped BFO comparison. The data have been adopted from ref. [9,31] for comparison purposes under a Creative Commons Attribution 4.0 International License.

The photoelectrochemical performance of Y-BFO and BFO films grown on Nb-STO substrates by Pulsed Laser Deposition technique, as a function of their thicknesses, was investigated as well [25]. It was observed that the FWHM values of the thicker Y-BFO films are higher than those obtained for the thinnest film, meaning that the mosaicity of thin films is less influenced by defects and dislocations and the parallel coherence length is maintained on higher nanodomains. The fully strained state is obtained for the thinnest Y-BFO film (22 nm), which shows the highest out-of-plane parameter and an in-plane parameter almost equal to the lattice parameter of the Nb-STO substrate. The increase in film thickness is accompanied by a structural relaxation of the grown film and at 145 nm Y-BFO can be considered fully relaxed. The highest photoelectrochemical activity was obtained for the thinnest Y-BFO/STON film with a resulting photocurrent density of  $0.72 \text{ mA}/\text{cm}^2$  at 1.4 V vs. RHE. The photocurrent density decreases with the increase in the film thickness, while all samples show excellent photoelectrochemical stabilities in time [25].

## 2.2. $\text{LaFeO}_3$ (LFO)

The photoelectrochemical properties of LFO thin films have been investigated. The photocatalyst was irradiated with a light source of 400 W output power, and an amount of  $3315 \mu\text{mol g}^{-1} \text{h}^{-1}$  of hydrogen was generated [37]. Nanoporous p-type LFO photocathodes prepared by electrochemical co-deposition show high resistance to photocorrosion [53]. Plasmonic Ag and Ni nanoparticles were integrated into LFO through spin coating, the resulting photocathode showing enhanced absorption and photocatalytic properties due to the surface plasmon resonances. The generated volume of hydrogen obtained with the modified LFO electrodes is several times higher than that obtained for the bare LFO [41,42]. Highly oriented (001) heteroepitaxial LFO films were grown on STON substrates by PLD at different oxygen partial pressures, and the influence of oxygen content on their photoelectrochemical properties was evaluated [34]. A small tensile stress along the c-axis was evidenced for LFO films prepared at oxygen pressures lower than 0.9 mbar, and at  $P_{\text{O}_2} \geq 0.9$  mbar no noticeable structural strain was observed. The highest crystalline quality with a very sharp interface and flat surface is obtained for LFO film grown at 0.6 mbar  $\text{O}_2$ . The same sample shows the lowest values of the microstrain and mean mosaic tilt angles, and giant lateral coherence length. The maximum photocurrent is obtained for LFO/STON film prepared at 0.6 mbar due to its high oxygen content and low number of oxygen vacancies, which decrease the free charge carrier's recombination [34].

The photoelectrochemical efficiency is strongly affected by the structural properties of prepared LFO films. The perpendicular microstrain, which is a measure of defects along the growth direction, decreases with the increase in the oxygen partial pressure, and the IPCE efficiency is improved with the defect's concentration decrease, as can be seen in Figure 2 [34]. Above 0.6 mbar  $\text{O}_2$ , this tendency is changed, the microstrain severely increases and the IPCE efficiency is diminished. Mean mosaic tilt angles follow the same trend with the oxygen partial pressure as the perpendicular microstrain, as presented in Figure 3 [34].

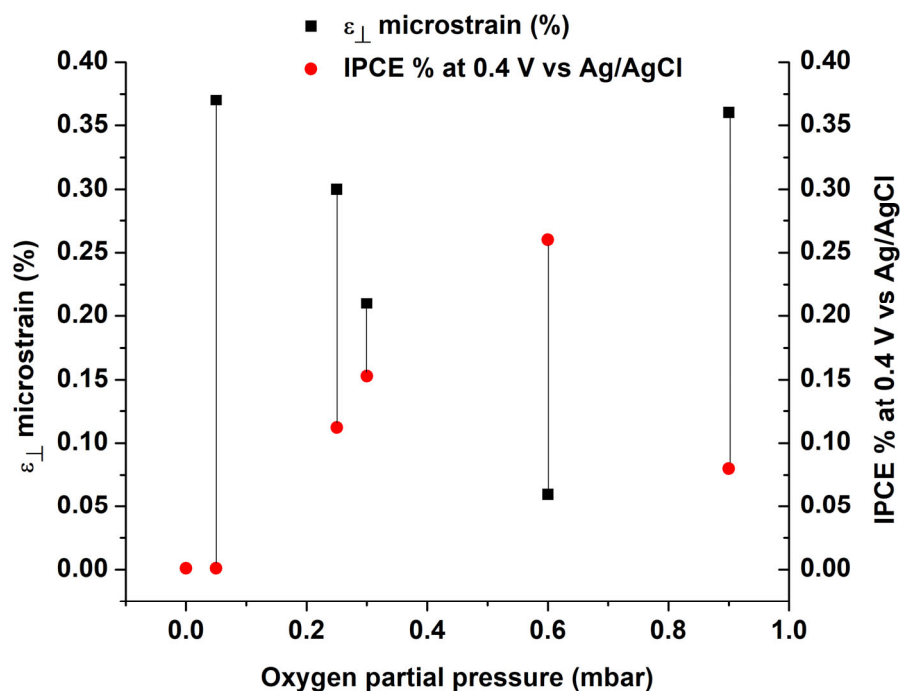
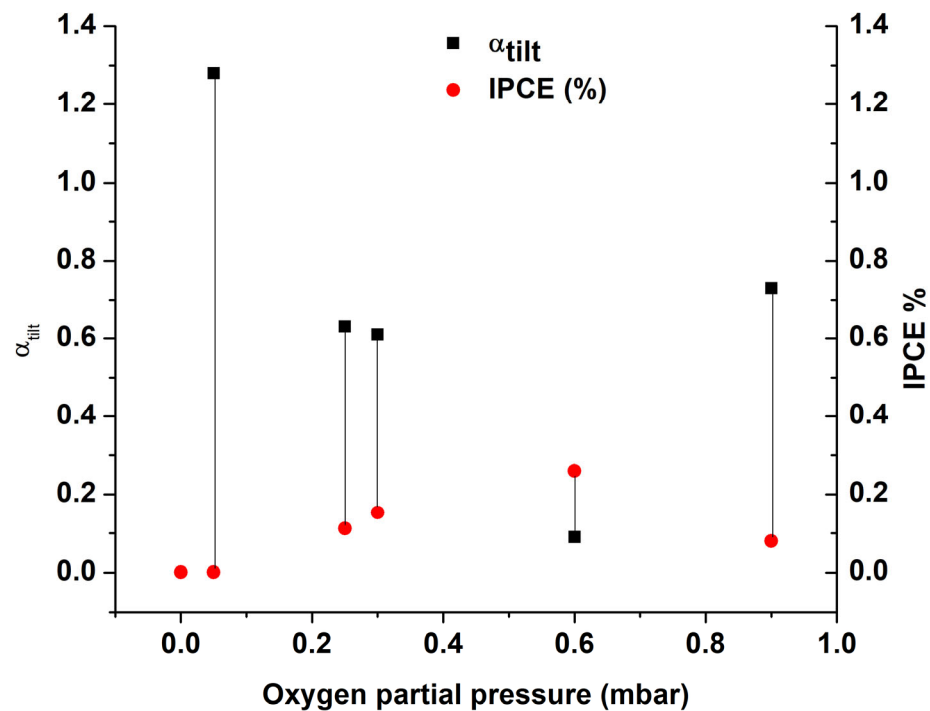


Figure 2. The microstrain and IPCE percentages as a function of  $P_{\text{O}_2}$  [34].



**Figure 3.** The  $\alpha_{\text{tilt}}$  and IPCE efficiencies as a function of  $P_{\text{O}_2}$  [34].

A detailed study related to the influence of ultra-thin LFO/STON film thicknesses (2–25 nm) on their photoelectrochemical performance was reported [54]. During the cyclic voltammetry measurements, all LFO films show asymmetric currents with regard to forward and reverse potentials, this behavior being correlated to the n-p heterojunction created between the substrate and film. All samples show a photoanodic response; the photocathodic response is observed, instead, only for samples having 10–25 nm thicknesses [54]. The effect of thicker LFO films (14–192 nm) prepared by PLD on their photoelectrochemical performances was also reported [55]. The out-of-plane parameters increase with the film thickness, and this increase is assisted by a decrease in the lattice expansion, in contrast to bulk LFO, as presented in Figure 4. Supplementarily, the incident photon-to-current efficiencies decrease with the increase in film thickness. The onset potentials are, also, affected by the thicknesses of LFO films, as can be seen in Figure 5. For thinner films, the onset potential is higher and it decreases with the increase in the film thickness [55].

An excellent quality of LFO films is obtained, especially for the thinner films, the thicker films showing a more defective structure. Several crevasse-like defects filled with amorphous material which penetrate the film to a depth of 8–9 nm are observed for film having 25 nm thickness, the film-substrate interface region being defectless. For the thickest film (140 nm), some nanopyramid-like structures appear, and these are detrimental for the photoelectrochemical activity of LFO films, because they act as leakage channels, increasing the free charge recombination.

These tendencies, namely the crevasse-like defect appearance, have been also confirmed from the structural point of view by HR-TEM analyses reported on LFO/STON thin films with different thicknesses, as can be seen from Figure 6 [55]. In Figure 6a,b, the appearance of the defects (noted “c”, for crevasse-like) for the LFO films above 15–16 nm is visible and is leading to nanopyramid structures toward the film surface in the case of thicker LFO/STON films (roughly 130 nm). The 130 nm-thick films exhibit a highly disordered structure, with defects stretching into the film volume and limiting the pyramid structure expansion.

The highest photoelectrochemical performance was obtained for the thinnest film with the maximum value of photocurrent of  $J_{\text{ph}} = 1.23 \text{ mA/cm}^2$  at 1.6 V applied potential vs. RHE [42]. Moreover, unassisted hydrogen was produced for the thinnest film, an

amount of  $6.5 \mu\text{mole}/\text{cm}^2$  of hydrogen being produced after 4 h [55]. Both LFO and Y-BFO films prepared by using an ArF excimer laser (193 nm) show better photoelectrochemical performances than LFO films prepared by a KrF excimer laser (248 nm), as can be observed in Figure 7. However, the highest photogenerated current is obtained for the LFO film having a thickness of 14 nm, no BFO film with the same thickness being available for comparison.

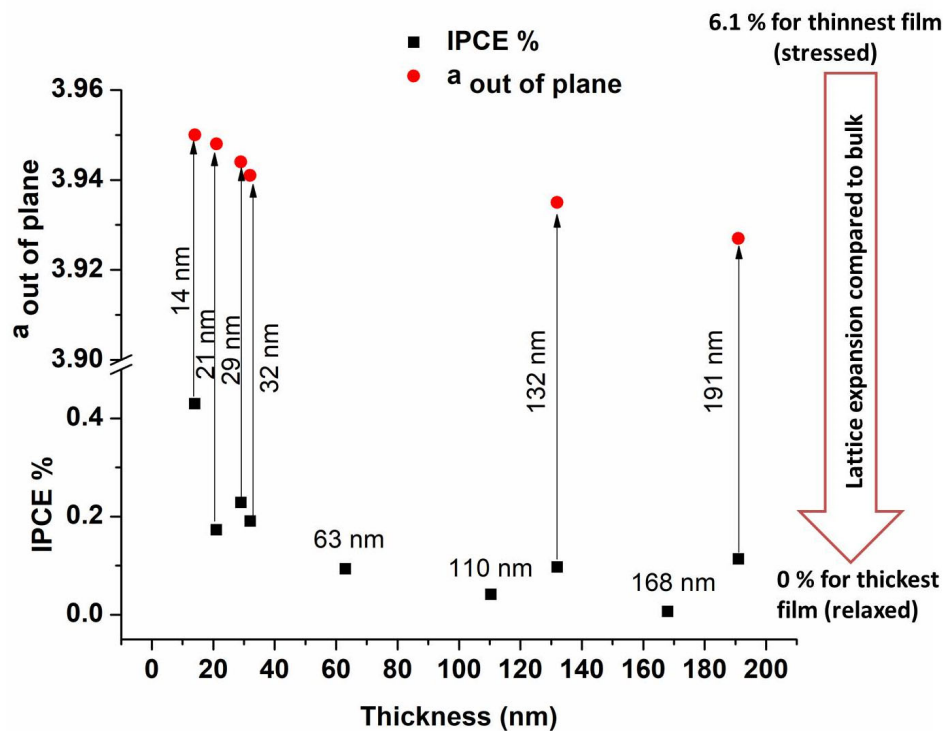


Figure 4. The out-of-plane parameters and IPCE efficiencies as a function of thickness.

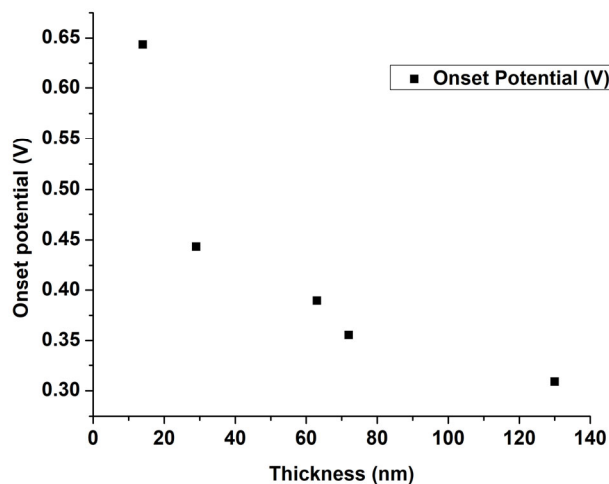
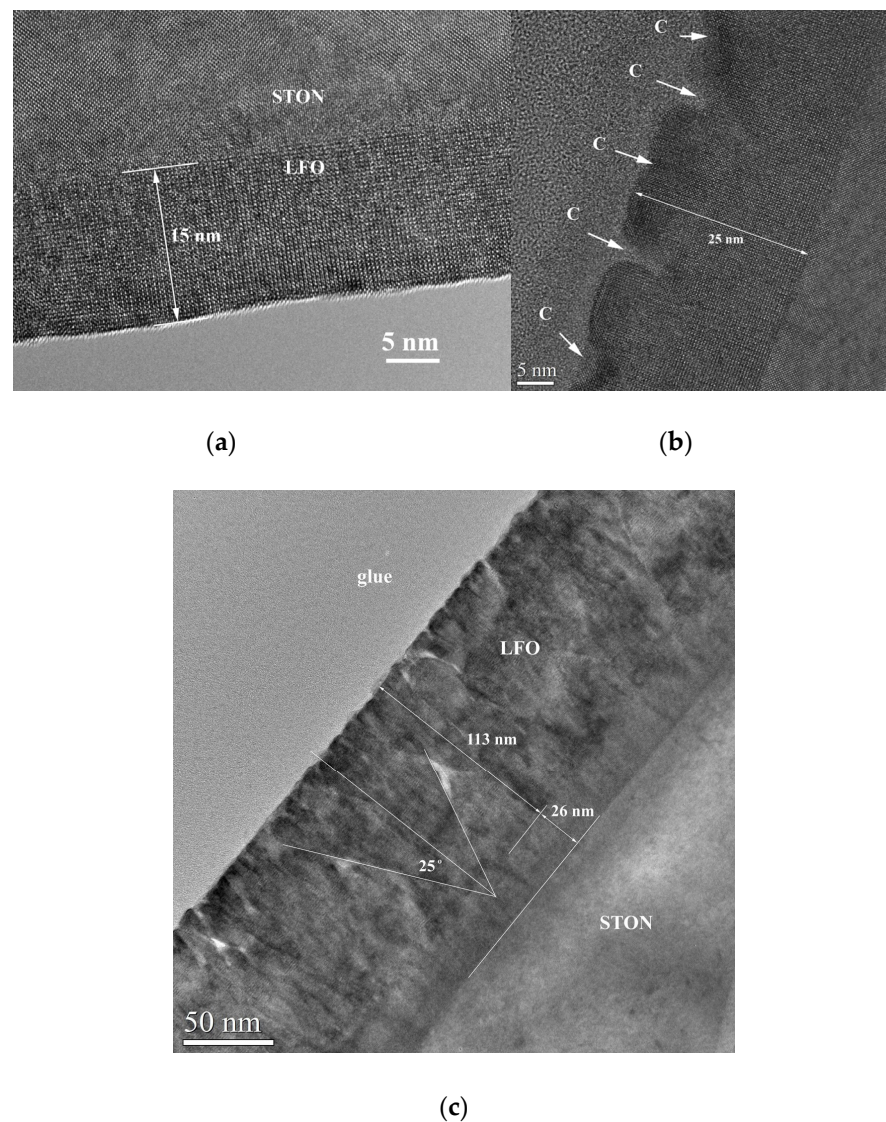


Figure 5. Onset potentials as a function of LFO film thicknesses.



**Figure 6.** (a) High-resolution TEM images for thin (15 nm) LFO/STON sample; (b) the crevasse-like defects appearance noticed from the high-resolution TEM images for thin (25 nm) LFO/STON sample; (c) low-magnification TEM image for thick (132 nm) LFO/STON sample. Figure reprinted from ref. [55] under a Creative Commons Attribution 4.0 International License.

Excellent photocatalytic activities were obtained in an artificial Z-scheme system with the decoration of a LFO-graphitic carbon nitride ( $g\text{-C}_3\text{N}_4$ )-BFO photocatalyst with Au nanoparticles. A huge amount of hydrogen ( $698.4 \mu\text{mol}\cdot\text{h}^{-1}\cdot\text{g}^{-1}$ ) was generated in this configuration due to the high surface plasmon resonance (SPR) effect of Au nanoparticles [56].

LFO films with different thicknesses (33–120 nm) on Nb-STO substrates were grown by PLD, starting from a ceramic LFO target. The electrolyte solutions in which photoelectrodes are tested play an important role in the overall photoelectrochemical activity. The photoelectrochemical performance of LFO films in different electrolytes solutions is reported. In an alkaline electrolyte with  $\text{pH} = 13.5$  (0.5 M NaOH), the generated current density under dark conditions is almost 0 along the entire potential range, as presented in Figure 8a. The values of current densities obtained without illumination in an acidic electrolyte,  $\text{pH} = 5.6$  ( $\text{Na}_2\text{SO}_4$  1M adjusted with  $\text{H}_2\text{SO}_4$  0.5 M), are much higher for all thicknesses in both cathodic and anodic regions (Figure 8b). Even though, in some cases, the values are almost six times higher than those obtained in alkaline conditions, the catalytic activity in the absence of light can be considered negligible.

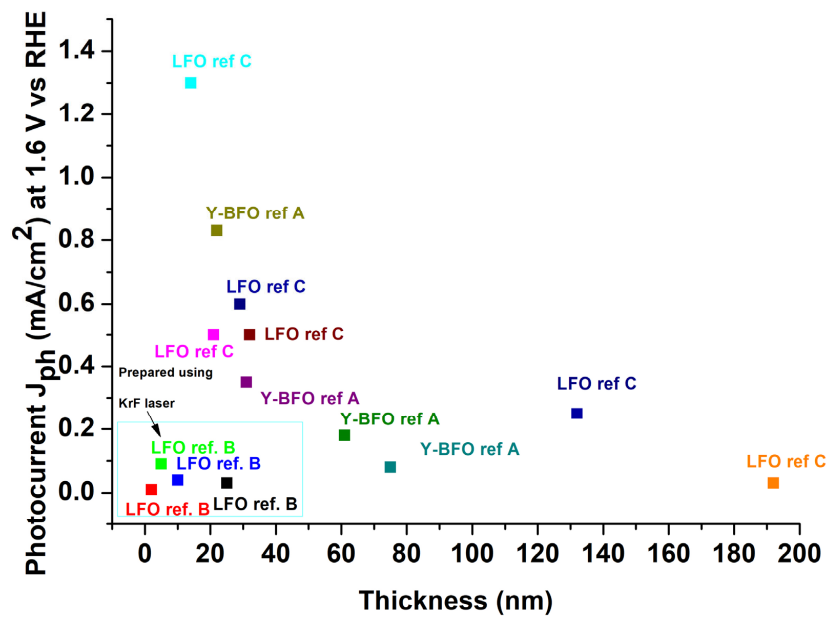


Figure 7. Photoanodic current as a function of film thickness for different LFO and Y-BFO films prepared by KrF and ArF excimer lasers; ref A: [25]; ref B: [54]; ref C: [55].

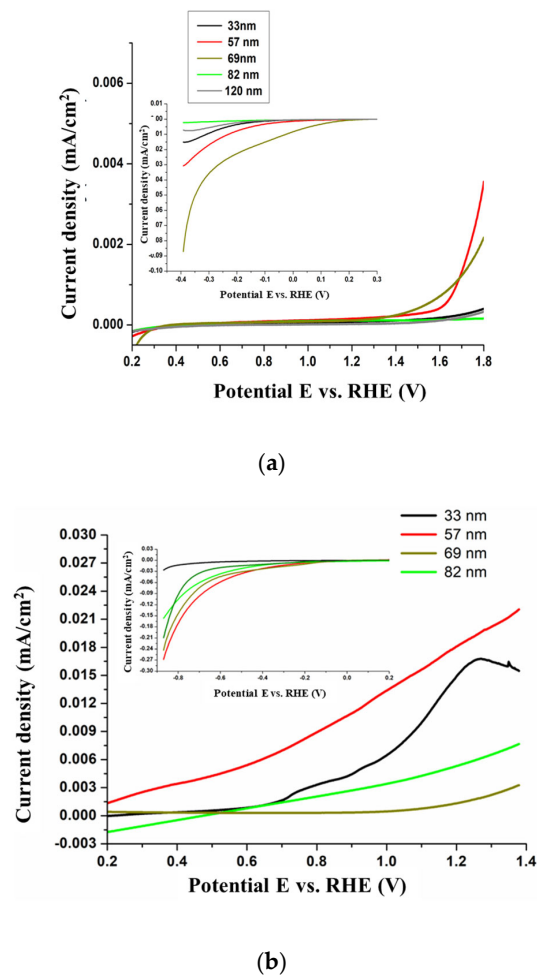
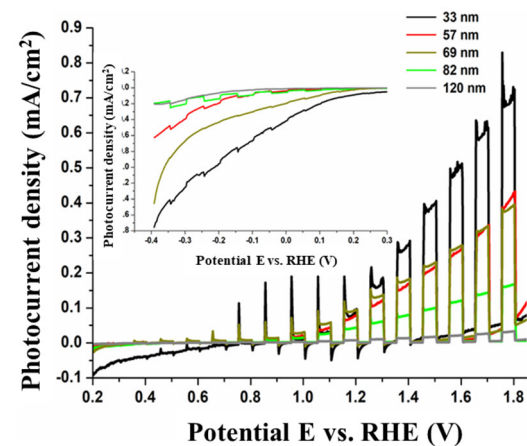
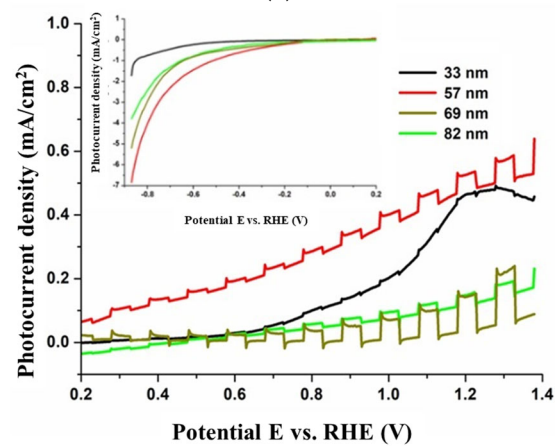


Figure 8. Current density obtained under dark conditions in (a) alkaline medium and (b) acidic medium for LFO films having different thicknesses.

During the potentiodynamic measurements in alkaline conditions, both photocathodic and photoanodic currents are observed, the intensities of oxidation photocurrents being much higher (Figure 9a). The highest photocurrent density is obtained for the thinnest LFO film with a value of around  $0.75 \text{ mA/cm}^2$  at  $1.8 \text{ V}$  vs. RHE, and it decreases with the increase in film thickness. This behavior is due to the more defective structure of thicker films, these defects acting as recombination traps for photogenerated electrons and positive holes, as already discussed earlier in this review. In an acidic medium, the photoelectrochemical response of LFO films is completely different, only photooxidation activity being observed (Figure 9b). Moreover, the performance of the thinnest LFO film is almost absent, the highest response being obtained for the film with  $69 \text{ nm}$  thickness. The leakage currents severely increase during the irradiation procedure, excepting the same sample with  $69 \text{ nm}$  thickness.



(a)



(b)

**Figure 9.** Potentiodynamic measurements in (a) alkaline medium and (b) acidic medium for LFO films having different thicknesses.

The potentiostatic measurements in a sodium hydroxide solution are presented in Figure 10a, where, as can be seen, all LFO films show excellent stabilities after 15 min of chopped irradiation. The photocurrent peaks are defined by moderate current spikes which can be correlated to a rapid electron-hole recombination. The spike intensities are severely higher in the acidic electrolyte, meaning that the recombination of charge carriers is much higher; this fact can be also seen in the height of photocurrent peaks, which is very small. The stabilities of LFO films are also affected in acidic solution, the photocurrent being altered in time (Figure 10b).

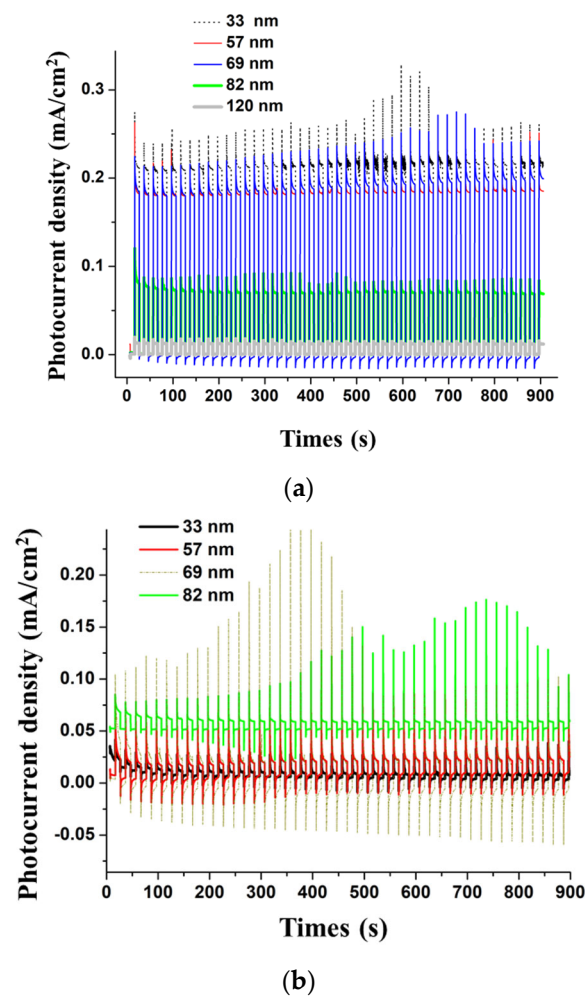


**Figure 10.** Potentiostatic measurements at 1.4 V vs. RHE in (a) alkaline medium and (b) acidic medium for LFO films having different thicknesses.

### 3. Conclusions

In summary, we have discussed the correlations between the structural strain in perovskite-like thin films and their functional properties. Different classes of lead-free materials have been examined.

BFO, a lead-free multiferroic perovskite, is one of the most studied materials due to its excellent electrical properties, high Curie temperature ( $T_C \sim 830$  °C), Néel temperature ( $T_N \sim 370$  °C) and photoelectrochemical activities. The strain induced in the BFO structure is an important factor, which severely governs its physicochemical properties. For BFO-based materials, a high piezoelectric coefficient  $d_{33}$ , huge remnant polarization and ferroelectricity, as well as very low leakage current density, were obtained for the most stressed structures. The rare earth doping of BFO films (deposited by PLD) induces huge in-plane dielectric permittivity ( $\cong 2500$ ) and low dielectric loss ( $< 0.01$ ). The formation of tilted stripe nanodomain structures with monoclinic symmetry, where the compressive and tensile strains alternate, is also noticed. The photoelectrochemical performances of Y-doped BFO are strongly influenced by film thicknesses, the highest photoanodic current being obtained for the most stressed sample (the thinnest one).

LFO exhibits photocatalytic properties, especially due to its absorption in the visible range, increased photostability, as well as high stability in both reducing and oxidizing chemical media. It is mainly used as a photocathode, but, depending on its synthesis method, it can possess an n-type semiconductor character with an important photoanodic response. The decoration of LFO base materials with precious metals (e.g., Au, Ag) was demonstrated to be an excellent method to further improve their absorption and photocat-

alytic properties, this happening due to the surface plasmon resonance effect. The oxygen content in LFO films plays an important role in their photoelectrochemical performances. The highest crystalline quality with a very sharp interface and flat surface is obtained for LFO film grown by Pulsed Laser Deposition at a specific oxygen partial pressure during deposition (0.6 mbar O<sub>2</sub>). The same sample shows the lowest values of microstrain and mean mosaic tilt angles and giant lateral coherence length. The maximum photocurrent is obtained for LFO/STON film prepared at 0.6 mbar, due to its high oxygen content and low number of oxygen vacancies, which decrease the free charge carriers recombination. The photoelectrochemical activities also vary with the film thicknesses. An excellent quality of LFO films is obtained, especially for the thinner films, the thicker films showing a more defective structure. The presence of several crevasse-like defects filled with amorphous material, which penetrate the film to a depth of 8–9 nm, is evidenced for film having 25 nm thickness, the film-substrate interface region being defectless. For the thickest film (130 nm), some nanopyramid-like structures appear, and these are detrimental for the photoelectrochemical activity of LFO films, because they act as leakage channels increasing the free charge recombination.

**Author Contributions:** Conceptualization, F.C. and N.D.S.; investigation, F.A., V.I., M.D. and R.B.; writing—original draft preparation, F.A. and N.D.S.; writing—review and editing, F.A., N.D.S., F.C. and M.D.; funding acquisition, N.D.S. All authors have read and agreed to the published version of the manuscript.

**Funding:** This research was funded by UEFISCDI, through the PN-III-P4-PCE-2021-1906 PCE97/2022 project.

**Data Availability Statement:** The data presented in this study are available in this article.

**Conflicts of Interest:** The authors declare no conflict of interest.

## References

1. Panda, P.K.; Sahoo, B.; Ramakrishna, J.; Manoj, B.; Rao, D.S.D.P. Recent Studies on Vibrational Energy Harvesting of PZT Materials. *Mater. Today Proc.* **2018**, *5*, 21512–21516. [[CrossRef](#)]
2. Jaffe, B.; Roth, R.S.; Marzullo, S. Piezoelectric Properties of Lead Zirconate-Lead Titanate Solid-Solution Ceramics. *J. Appl. Phys.* **1954**, *25*, 809–810. [[CrossRef](#)]
3. Kimura, M.; Ando, A.; Maurya, D.; Priya, S. Lead Zirconate Titanate-Based Piezoceramics. In *Advanced Piezoelectric Materials*; Elsevier: Amsterdam, The Netherlands, 2017; pp. 95–126. [[CrossRef](#)]
4. Lines, M.E.; Glass, A.M.; Lines, M.E.; Glass, A.M. Principles and Applications of Ferroelectrics and Related Materials. In *Oxford Classic Texts in the Physical Sciences*; Oxford University Press: Oxford, NY, USA, 2001.
5. Anand, S.; Arockiarajan, A. Temperature dependent ferroelectric and ferroelastic behaviour of PZT wafers. *Ceram. Int.* **2016**, *42*, 15517–15529. [[CrossRef](#)]
6. Boerasu, I.; Pintilie, L.; Pereira, M.; Vasilevskiy, M.I.; Gomes, M.J.M. Competition between ferroelectric and semiconductor properties in Pb(Zr<sub>0.65</sub>Ti<sub>0.35</sub>)O<sub>3</sub> thin films deposited by sol–gel. *J. Appl. Phys.* **2003**, *93*, 4776–4783. [[CrossRef](#)]
7. Baraskar, B.G.; Kadhane, P.S.; Darvade, T.C.; James, A.R.; Kambale, R.C. BaTiO<sub>3</sub>-Based Lead-Free Electroceramics with Their Ferroelectric and Piezoelectric Properties Tuned by Ca<sup>2+</sup>, Sn<sup>4+</sup> and Zr<sup>4+</sup> Substitution Useful for Electrostrictive Device Application. In *Ferroelectrics and Their Applications*; Irzaman, H., Ed.; InTech: Orlando, FL, USA, 2018. [[CrossRef](#)]
8. Scarisoreanu, N.D.; Craciun, F.; Dinescu, M.; Ion, V.; Andrei, A.; Moldovan, A.; Teodorescu, V.; Ghica, C.; Birjega, R. Laser processing of nanostructures: Enhancing functional properties of lead-free perovskite nanostructures through chemical pressure and epitaxial strain. In *Functional Nanostructured Interfaces for Environmental and Biomedical Applications*; Elsevier: Amsterdam, The Netherlands, 2019; pp. 113–152. [[CrossRef](#)]
9. Scarisoreanu, N.D.; Craciun, F.; Birjega, R.; Ion, V.; Teodorescu, V.S.; Ghica, C.; Negrea, R.; Dinescu, M. Joining Chemical Pressure and Epitaxial Strain to Yield Y-doped BiFeO<sub>3</sub> Thin Films with High Dielectric Response. *Sci. Rep.* **2016**, *6*, 25535. [[CrossRef](#)] [[PubMed](#)]
10. Fujino, S.; Murakami, M.; Anbusathaiah, V.; Lim, S.-H.; Nagarajan, V.; Fennie, C.J.; Wuttig, M.; Salamanca-Riba, L.; Takeuchi, I. Combinatorial discovery of a lead-free morphotropic phase boundary in a thin-film piezoelectric perovskite. *Appl. Phys. Lett.* **2008**, *92*, 202904. [[CrossRef](#)]
11. Cheng, C.-J.; Borisevich, A.Y.; Kan, D.; Takeuchi, I.; Nagarajan, V. Nanoscale Structural and Chemical Properties of Antipolar Clusters in Sm-Doped BiFeO<sub>3</sub> Ferroelectric Epitaxial Thin Films. *Chem. Mater.* **2010**, *22*, 2588–2596. [[CrossRef](#)]
12. Kan, D.; Pálková, L.; Anbusathaiah, V.; Cheng, C.J.; Fujino, S.; Nagarajan, V.; Rabe, K.M.; Takeuchi, I. Universal Behavior and Electric-Field-Induced Structural Transition in Rare-Earth-Substituted BiFeO<sub>3</sub>. *Adv. Funct. Mater.* **2010**, *20*, 1108–1115. [[CrossRef](#)]

13. Yang, C.-H.; Kan, D.; Takeuchi, I.; Nagarajan, V.; Seidel, J. Doping BiFeO<sub>3</sub>: Approaches and enhanced functionality. *Phys. Chem. Chem. Phys.* **2012**, *14*, 15953. [[CrossRef](#)]
14. Singh, V.; Sharma, S.; Dwivedi, R.K.; Kumar, M.; Kotnala, R.K. Multiferroic and optical properties of Pr-substituted bismuth ferrite ceramics: Multiferroic and optical properties of bismuth ferrite ceramics. *Phys. Status Solidi A* **2013**, *210*, 1442–1447. [[CrossRef](#)]
15. Yan, Z.; Wang, K.F.; Qu, J.F.; Wang, Y.; Song, Z.T.; Feng, S.L. Processing and properties of Yb-doped BiFeO<sub>3</sub> ceramics. *Appl. Phys. Lett.* **2007**, *91*, 082906. [[CrossRef](#)]
16. Yuan, G.L.; Baba-Kishi, K.Z.; Liu, J.; Or, S.W.; Wang, Y.P.; Liu, Z.G. Multiferroic Properties of Single-Phase Bi<sub>0.85</sub>La<sub>0.15</sub>FeO<sub>3</sub> Lead-Free Ceramics. *J. Am. Ceram. Soc.* **2006**, *89*, 3136–3139. [[CrossRef](#)]
17. Kumar, M.; Yadav, K.L. Study of room temperature magnetoelectric coupling in Ti substituted bismuth ferrite system. *J. Appl. Phys.* **2006**, *100*, 074111. [[CrossRef](#)]
18. Xu, Q.; Zai, H.; Wu, D.; Qiu, T.; Xu, M.X. The magnetic properties of Bi(Fe<sub>0.95</sub>Co<sub>0.05</sub>)O<sub>3</sub> ceramics. *Appl. Phys. Lett.* **2009**, *95*, 112510. [[CrossRef](#)]
19. Jin, L.; Luo, W.B.; Qing, X.; Shuai, Y.; Yang, C.; Wu, C.G.; Zhang, W.L. Nd doping effects on the multifunction properties of BiFeO<sub>3</sub>. *Mater. Res. Innov.* **2015**, *19*, s35–s39. [[CrossRef](#)]
20. Lin, T.; Shen, C.; Kao, C.; Chang, C.; Wang, C.; Tu, C. Structural evolution, ferroelectric, and nanomechanical properties of Bi<sub>1-x</sub>Sm<sub>x</sub>FeO<sub>3</sub> films ( $x = 0.05$ – $0.16$ ) on glass substrates. *J. Alloys Compd.* **2019**, *787*, 397–406. [[CrossRef](#)]
21. Pei, W.; Chen, J.; You, D.; Zhang, Q.; Li, M.; Lu, Y.; Fu, Z.; He, Y. Enhanced photovoltaic effect in Ca and Mn co-doped BiFeO<sub>3</sub> epitaxial thin films. *Appl. Surf. Sci.* **2020**, *530*, 147194. [[CrossRef](#)]
22. Wang, J.; Neaton, J.B.; Zheng, H.; Nagarajan, V.; Ogale, S.B.; Liu, B.; Viehland, D.; Vaithyanathan, V.; Schlom, D.G.; Waghmare, U.V.; et al. Epitaxial BiFeO<sub>3</sub> Multiferroic Thin Film Heterostructures. *Science* **2003**, *299*, 1719–1722. [[CrossRef](#)]
23. Yan, Q.; Rinke, P.; Scheffler, M.; Van de Walle, C.G. Strain effects in group-III nitrides: Deformation potentials for AlN, GaN, and InN. *Appl. Phys. Lett.* **2009**, *95*, 121111. [[CrossRef](#)]
24. Baek, S.-H.; Lee, H.-J.; Lee, S.-N. High-performance flat-type InGaN-based light-emitting diodes with local breakdown conductive channel. *Sci. Rep.* **2019**, *9*, 11053. [[CrossRef](#)]
25. Haydous, F.; Scarisoreanu, N.D.; Birjega, R.; Ion, V.; Lippert, T.; Dumitrescu, N.; Moldovan, A.; Andrei, A.; Teodorescu, V.S.; Ghica, C.; et al. Rolling dopant and strain in Y-doped BiFeO<sub>3</sub> epitaxial thin films for photoelectrochemical water splitting. *Sci. Rep.* **2018**, *8*, 15826. [[CrossRef](#)]
26. Lei, Y.; Zhang, Y.; Ding, W.; Yu, L.; Zhou, X.; Wu, C.-M.L. Preparation and photoelectrochemical properties of BiFeO<sub>3</sub>/BiOI composites. *RSC Adv.* **2020**, *10*, 26658–26663. [[CrossRef](#)] [[PubMed](#)]
27. Fan, Z.; Sun, K.; Wang, J. Perovskites for photovoltaics: A combined review of organic–inorganic halide perovskites and ferroelectric oxide perovskites. *J. Mater. Chem. A* **2015**, *3*, 18809–18828. [[CrossRef](#)]
28. Harwood, M.G.; Popper, P.; Rushman, D.F. Curie Point of Barium Titanate. *Nature* **1947**, *160*, 58–59. [[CrossRef](#)] [[PubMed](#)]
29. Liu, W.; Ren, X. Large Piezoelectric Effect in Pb-Free Ceramics. *Phys. Rev. Lett.* **2009**, *103*, 257602. [[CrossRef](#)]
30. Cordero, F.; Craciun, F.; Dinescu, M.; Scarisoreanu, N.; Galassi, C.; Schranz, W.; Soprunyuk, V. Elastic response of  $(1 - x)\text{Ba}(\text{Ti}_{0.8}\text{Zr}_{0.2})\text{O}_3 - x(\text{Ba}_{0.7}\text{Ca}_{0.3})\text{TiO}_3$  ( $x = 0.45$ – $0.55$ ) and the role of the intermediate orthorhombic phase in enhancing the piezoelectric coupling. *Appl. Phys. Lett.* **2014**, *105*, 232904. [[CrossRef](#)]
31. Scarisoreanu, N.D.; Craciun, F.; Moldovan, A.; Ion, V.; Birjega, R.; Ghica, C.; Negrea, R.F.; Dinescu, M. High Permittivity  $(1 - x)\text{Ba}(\text{Zr}_{0.2}\text{Ti}_{0.8})\text{O}_3 - x(\text{Ba}_{0.7}\text{Ca}_{0.3})\text{TiO}_3$  ( $x = 0.45$ ) Epitaxial Thin Films with Nanoscale Phase Fluctuations. *ACS Appl. Mater. Interfaces* **2015**, *7*, 23984–23992. [[CrossRef](#)]
32. Ion, V.; Craciun, F.; Scarisoreanu, N.D.; Moldovan, A.; Andrei, A.; Birjega, R.; Ghica, C.; Di Pietrantonio, F.; Cannata, D.; Benetti, M.; et al. Impact of thickness variation on structural, dielectric and piezoelectric properties of (Ba,Ca)(Ti,Zr)O<sub>3</sub> epitaxial thin films. *Sci. Rep.* **2018**, *8*, 2056. [[CrossRef](#)]
33. Mukhopadhyay, K.; Mahapatra, A.; Chakrabarti, P. Multiferroic behavior, enhanced magnetization and exchange bias effect of Zn substituted nanocrystalline LaFeO<sub>3</sub> (La(1-x)Zn<sub>x</sub>FeO<sub>3</sub>,  $x=0.10$ , and  $0.30$ ). *J. Magn. Magn. Mater.* **2013**, *329*, 133–141. [[CrossRef](#)]
34. Andrei, F.; Boerasu, I.; Birjega, R.; Moldovan, A.; Dinescu, M.; Ion, V.; Mihailescu, C.; Scarisoreanu, N.D.; Leca, V. The effects of the oxygen content on the photoelectrochemical properties of LaFeO<sub>3</sub> perovskite thin films obtained by pulsed laser deposition. *Appl. Phys. A* **2019**, *125*, 807. [[CrossRef](#)]
35. Bi, L.; Kim, H.-S.; Dionne, G.F.; Ross, C.A.; Paik, H.; Park, Y.C. Orientation control and self-assembled nanopillar structure of LaFeO<sub>3</sub> films epitaxially grown on SrTiO<sub>3</sub>(001) substrates. *Appl. Phys. Lett.* **2009**, *95*, 121908. [[CrossRef](#)]
36. Steele, B.C.H.; Heinzl, A. Materials for fuel-cell technologies. *Nature* **2001**, *414*, 345–352. [[CrossRef](#)] [[PubMed](#)]
37. Tijare, S.N.; Joshi, M.V.; Padole, P.S.; Mangrulkar, P.A.; Rayalu, S.S.; Labhsetwar, N.K. Photocatalytic hydrogen generation through water splitting on nano-crystalline LaFeO<sub>3</sub> perovskite. *Int. J. Hydrog. Energy* **2012**, *37*, 10451–10456. [[CrossRef](#)]
38. Celorrio, V.; Bradley, K.; Weber, O.J.; Hall, S.R.; Fermín, D.J. Photoelectrochemical Properties of LaFeO<sub>3</sub> Nanoparticles. *ChemElectroChem* **2014**, *1*, 1667–1671. [[CrossRef](#)]
39. Margellou, A.; Papadas, I.; Petrakis, D.; Armatas, G. Development of enhanced surface area LaFeO<sub>3</sub> perovskites using amino acids as templating agents. *Mater. Res. Bull.* **2016**, *83*, 491–501. [[CrossRef](#)]
40. Freeman, E.; Kumar, S.; Celorrio, V.; Park, M.S.; Kim, J.H.; Fermín, D.J.; Eslava, S. Strategies for the deposition of LaFeO<sub>3</sub> photocathodes: Improving the photocurrent with a polymer template. *Sustain. Energy Fuels* **2020**, *4*, 884–894. [[CrossRef](#)]
41. Catalan, G.; Scott, J.F. Physics and Applications of Bismuth Ferrite. *Adv. Mater.* **2009**, *21*, 2463–2485. [[CrossRef](#)]

42. Béa, H.; Gajek, M.; Bibes, M.; Barthélémy, A. Spintronics with multiferroics. *J. Phys. Condens. Matter* **2008**, *20*, 434221. [[CrossRef](#)]
43. Chiu, S.-J.; Liu, Y.-T.; Lee, H.-Y.; Yu, G.-P.; Huang, J.-H. Strain enhanced ferroelectric properties of multiferroic BiFeO<sub>3</sub>/SrTiO<sub>3</sub> superlattice structure prepared by radio frequency magnetron sputtering. *Thin Solid. Film.* **2013**, *539*, 75–80. [[CrossRef](#)]
44. Kubicek, M.; Cai, Z.; Ma, W.; Yildiz, B.; Hutter, H.; Fleig, J. Tensile Lattice Strain Accelerates Oxygen Surface Exchange and Diffusion in La<sub>1-x</sub>Sr<sub>x</sub>CoO<sub>3-δ</sub> Thin Films. *ACS Nano* **2013**, *7*, 3276–3286. [[CrossRef](#)]
45. Tealdi, C.; Heath, J.; Islam, M.S. Feeling the strain: Enhancing ionic transport in olivine phosphate cathodes for Li- and Na-ion batteries through strain effects. *J. Mater. Chem. A* **2016**, *4*, 6998–7004. [[CrossRef](#)]
46. Himcinschi, C.; Vrejoiu, I.; Friedrich, M.; Nikulina, E.; Ding, L.; Cobet, C.; Esser, N.; Alexe, M.; Rafaja, D.; Zahn, D.R.T. Substrate influence on the optical and structural properties of pulsed laser deposited BiFeO<sub>3</sub> epitaxial films. *J. Appl. Phys.* **2010**, *107*, 123524. [[CrossRef](#)]
47. Kim, D.H.; Lee, H.N.; Biegalski, M.D.; Christen, H.M. Effect of epitaxial strain on ferroelectric polarization in multiferroic BiFeO<sub>3</sub> films. *Appl. Phys. Lett.* **2008**, *92*, 012911. [[CrossRef](#)]
48. Saito, K.; Ulyanenkova, A.; Grossmann, V.; Rössel, H.; Bruegemann, L.; Ohta, H.; Kurosawa, T.; Ueki, S.; Funakubo, H. Structural Characterization of BiFeO<sub>3</sub> Thin Films by Reciprocal Space Mapping. *Jpn. J. Appl. Phys.* **2006**, *45*, 7311. [[CrossRef](#)]
49. Chu, Y.; Zhan, Q.; Martin, L.W.; Cruz, M.P.; Yang, P.; Pabst, G.W.; Zavaliche, F.; Yang, S.; Zhang, J.; Chen, L.; et al. Nanoscale domain control in multiferroic BiFeO<sub>3</sub> thin films. *Adv. Mater.* **2006**, *18*, 2307–2311. [[CrossRef](#)]
50. Himcinschi, C.; Bhatnagar, A.; Talkenberger, A.; Barchuk, M.; Zahn, D.R.T.; Rafaja, D.; Kortus, J.; Alexe, M. Optical properties of epitaxial BiFeO<sub>3</sub> thin films grown on LaAlO<sub>3</sub>. *Appl. Phys. Lett.* **2015**, *106*, 012908. [[CrossRef](#)]
51. Liu, W.; Tan, G.; Ren, H.; Xia, A. Multiferroic BiFe<sub>1-x</sub>TM<sub>x</sub>O<sub>3</sub>/NiFe<sub>2</sub>O<sub>4</sub> (TM = Mn, Cr) thin films: Structural, electrical and magnetic properties. *J. Alloys Compd.* **2015**, *647*, 351–356. [[CrossRef](#)]
52. Zhao, J.; Lu, H.; Sun, J.; Shen, B. Thickness dependence of piezoelectric property of ultrathin BiFeO<sub>3</sub> films. *Phys. B Condens. Matter* **2012**, *407*, 2258–2261. [[CrossRef](#)]
53. Wheeler, G.P.; Choi, K.-S. Photoelectrochemical Properties and Stability of Nanoporous p-Type LaFeO<sub>3</sub> Photoelectrodes Prepared by Electrodeposition. *ACS Energy Lett.* **2017**, *2*, 2378–2382. [[CrossRef](#)]
54. May, K.J.; Fenning, D.P.; Ming, T.; Hong, W.T.; Lee, D.; Stoerzinger, K.A.; Biegalski, M.D.; Kolpak, A.M.; Shao-Horn, Y. Thickness-Dependent Photoelectrochemical Water Splitting on Ultrathin LaFeO<sub>3</sub> Films Grown on Nb:SrTiO<sub>3</sub>. *J. Phys. Chem. Lett.* **2015**, *6*, 977–985. [[CrossRef](#)]
55. Andrei, F.; Ion, V.; Birjega, R.; Dinescu, M.; Enea, N.; Pantelica, D.; Mihai, M.D.; Maraloiu, V.-A.; Teodorescu, V.S.; Marcu, I.-C.; et al. Thickness-Dependent Photoelectrochemical Water Splitting Properties of Self-Assembled Nanostructured LaFeO<sub>3</sub> Perovskite Thin Films. *Nanomaterials* **2021**, *11*, 1371. [[CrossRef](#)] [[PubMed](#)]
56. Arif, N.; Ma, Y.; Iqbal, M.A.; Zafar, M.N.; Liang, H.; Zhang, Q.; Zeng, Y.-J. Enhanced charge separation in dual Z-scheme Au decorated LaFeO<sub>3</sub>-g-C<sub>3</sub>N<sub>4</sub>-BiFeO<sub>3</sub> system for efficient H<sub>2</sub> production. *Fuel* **2023**, *336*, 126832. [[CrossRef](#)]

**Disclaimer/Publisher's Note:** The statements, opinions and data contained in all publications are solely those of the individual author(s) and contributor(s) and not of MDPI and/or the editor(s). MDPI and/or the editor(s) disclaim responsibility for any injury to people or property resulting from any ideas, methods, instructions or products referred to in the content.